Geophysical Journal International

Geophys. J. Int. (2010) **183,** 820–832 doi: 10.1111/j.1365-246X.2010.04725.x

Simulation of surface waves in porous media

Rolf Sidler,[1] José M. Carcione[2] and Klaus Holliger[1]

[1] *Institute of Geophysics, University of Lausanne,* CH-1015 *Lausanne, Switzerland. E-mail: rolf.sidler@unil.ch*
[2] *Istituto Nazionale di Oceanografia e di Geofisica Sperimentale (OGS), Borgo Grotta Gigante* 42c, 34010 *Sgonico, Trieste, Italy*

Accepted 2010 July 6. Received 2010 July 5; in original form 2010 February 9

SUMMARY

We present a novel numerical algorithm for the simulation of seismic wave propagation in porous media, which is particularly suitable for the accurate modelling of surface wave-type phenomena. The differential equations of motion are based on Biot's theory of poro-elasticity and solved with a pseudospectral approach using Fourier and Chebyshev methods to compute the spatial derivatives along the horizontal and vertical directions, respectively. The time solver is a splitting algorithm that accounts for the stiffness of the differential equations. Due to the Chebyshev operator the grid spacing in the vertical direction is non-uniform and characterized by a denser spatial sampling in the vicinity of interfaces, which allows for a numerically stable and accurate evaluation of higher order surface wave modes. We stretch the grid in the vertical direction to increase the minimum grid spacing and reduce the computational cost. The free-surface boundary conditions are implemented with a characteristics approach, where the characteristic variables are evaluated at zero viscosity. The same procedure is used to model seismic wave propagation at the interface between a fluid and porous medium. In this case, each medium is represented by a different grid and the two grids are combined through a domain-decomposition method. This wavefield decomposition method accounts for the discontinuity of variables and is crucial for an accurate interface treatment. We simulate seismic wave propagation with open-pore and sealed-pore boundary conditions and verify the validity and accuracy of the algorithm by comparing the numerical simulations to analytical solutions based on zero viscosity obtained with the Cagniard-de Hoop method. Finally, we illustrate the suitability of our algorithm for more complex models of porous media involving viscous pore fluids and strongly heterogeneous distributions of the elastic and hydraulic material properties.

Key words: Numerical solutions; Fractals and multifractals; Surface waves and free oscillations; Interface waves; Computational seismology; Wave propagation.

1 INTRODUCTION

A number of problems in environmental geophysics, seismic exploration, civil engineering, earthquake seismology, and non-destructive testing can be described by poro-elastic models consisting of an elastic matrix that is pervaded with partially interconnected fluid-filled cavities. Terzaghi (1923, 1943) was among the first to use this concept to describe the effective stress bearing on a saturated porous skeleton as the difference between total stress and the pore fluid pressure. Biot (1941) formulated a theory of soil consolidation using the same concept and extended it subsequently to describe wave propagation in porous media (Biot 1956a,b, 1962a,b). He predicted the existence of two kinds of compressional wave in a porous medium: the fast wave, for which the solid and fluid displacements are in phase, and the slow wave, for which the displacements are out of phase. The slow wave does not propagate through the medium at low frequencies as it becomes diffusive due to the dominating effect of fluid viscosity. In contrast, the slow wave is present at high frequencies where inertial effects dominate over those related to viscosity. Tangential slip at the pore boundaries takes place as a consequence of a thin boundary layer, compared to the pore size. The diffusive character of the slow wave makes its observation a difficult task and it took some time until the existence of the slow wave could officially be confirmed experimentally (Plona 1980; Chandler 1981; Van der Grinten *et al.* 1985), although its discovery prior to Biot's theoretical prediction passed almost unnoticed (Oura 1952; Johnson 1982; Carcione 2007). Geerstma & Smit (1961) showed that the slow wave contributes to the attenuation of the fast wave by mode conversion at inhomogeneities. This finding has recently again attracted attention in view of the increasing evidence that the distribution of rock physical parameters in general and seismic material properties in particular seem to be governed by remarkably uniform and universal fractal scaling laws (Hardy & Beier 1994; Holliger 1996; Turcotte 1997; Holliger & Goff 2003).

Surface waves and guided waves, and their propagation in porous media are of increasing interest for a variety of fields, notably in onshore and offshore civil engineering as well as in borehole

logging. Many seismic applications require sources and receivers to be placed at or near interfaces. The Rayleigh wave in a porous medium is composed of the fast *P* wave, the *S* wave, and the slow *P* wave. The underlying physics has been studied, for example, by Deresiewicz (1962), who found that the Rayleigh wave is a dissipative and dispersive phenomenon due to losses by mode conversion to the slow wave (Bourbié *et al.* 1987). Surface waves at a liquid–porous medium interface, such as for example the seafloor, can be classified into three kinds. A true surface wave corresponding to the generalization of the Scholte wave that travels slower than all the wave velocities, a pseudo-Scholte wave that travels with a velocity between the *S*-wave velocity, and the slow *P*-wave velocity, leaking energy to the slow wave, and a pseudo-Rayleigh wave, which becomes the classical Rayleigh wave if the liquid density goes to zero (Holland 1991; Edelman & Wilmanski 2002). For open-pore boundary conditions, the true surface wave exists for a limited range of material parameters, while for sealed-pore conditions this wave exists for all values of material parameters (Feng & Johnson 1983a,b). In a similar fashion to the slow *P* wave, the true surface wave is difficult to observe. Nagy (1992) observed a new surface wave in alcohol-saturated porous sintered glass. The conditions for the existence of this wave are a highly compressible superstrate fluid, such as air, a closed surface, due to surface tension in Nagy's experiments, and negligible viscosity of the saturating fluid.

In this paper, we present a numerical algorithm that allows for the accurate simulation of surface wave-type phenomena in porous media. The algorithm is based on a pseudospectral approach and allows for an explicit treatment of interfaces. A separate modelling domain is used for each medium and the wavefield at the interface is decomposed into an incoming and an outgoing field for each medium. This wavefield decomposition is based on characteristic variables that are evaluated for different boundary conditions (Carcione 1991, 1996a) and has the advantage that it accounts for variables that are non-continuous across interfaces and hence can not be correctly approximated with a gradient (Morency & Tromp 2008). The Chebyshev operator used in the vertical direction leads to a denser sampling in the vicinity of the interface, which is desirable for modelling surface wave propagation phenomena (Mittet 2002). Biot's (1956a,b) poro-elastic differential equations are stiff (Jain 1984) due to the presence of the diffusive slow mode at low frequencies. Therefore, the time integration is performed with a splitting method, where the stiff part of the differential equations is solved analytically and the regular part is solved by an explicit fourth-order Runge–Kutta algorithm (Carcione & Quiroga-Goode 1995).

By combining all the analytical and numerical approaches described above and adding the boundary equations for the extreme cases of open- and sealed-pores conditions we obtain a novel numerical tool that is especially well suited to investigate complex surface wave propagation phenomena in realistic porous media. We illustrate the accuracy of the developed modelling algorithm by comparing its results against analytical solutions and use it to explore the propagation of the various types of surface waves in response to variations in viscosity and interface flow impedance as well as strongly heterogeneous distributions of the hydraulic and elastic material parameters.

2 EQUATIONS OF MOTION

The equations describing the propagation of seismic waves in a porous medium combine the stress–strain relation and the Biot–Euler and Darcy–Euler equations (Biot 1962a,b; Carcione 1998, 2007). The velocity–stress formulation used in this study allows for the calculation of the particle velocity and stress components simultaneously.

2.1 Poro-elastic equations of motion

(i) Stress-strain relations: The constitutive equations for an inhomogeneous, isotropic poro-elastic medium under plane strain conditions are given by

$$\tau_{xx,t} = E_{\rm m} v_{x,x} + (E_{\rm m} - 2\mu_{\rm m}) v_{z,z} + \alpha M \epsilon + s_{xx}, \tag{1}$$

$$\tau_{zz,t} = (E_{\rm m} - 2\mu_{\rm m}) v_{x,x} + E_{\rm m} v_{z,z} + \alpha M \epsilon + s_{zz}. \tag{2}$$

$$\tau_{xz,t} = \mu_{\rm m}(v_{x,z} + v_{z,x}) + s_{xz}, \tag{3}$$

$$p_{2,t} = -M\epsilon + s_{f2}, \tag{4}$$

$$\epsilon = \alpha(v_{x,x} + v_{z,z}) + q_{x,x} + q_{z,z}, \tag{5}$$

where the subscripts x and z, and t refer to the principal axes of a 2-D Cartesian coordinate system and the time, respectively, τ_{xx}, τ_{zz}, and τ_{xz} are the total stress components, p_2 is the pore fluid pressure, v_x and v_z are the particle velocities in the solid, q_x and q_z are particle velocities in the fluid relative to the solid, and s_{xx}, s_{zz}, s_{xz}, and s_{f2} are components of the external sources.

A poro-elastic solid consists of a porous elastic frame, which is also referred to as the matrix, and the saturating pore fluid. The stiffness of the solid frame depends on the geometry of the pore space as well as the material which it is built of. A fluid-saturated medium is commonly referred as 'undrained' whereas the 'drained' state corresponds to the properties of the unsaturated frame. The elastic coefficients are given by

$$E_{\rm m} = K_{\rm m} + \frac{4}{3}\mu_{\rm m}, \tag{6}$$

$$M = \frac{K_{\rm s}^2}{D - K_{\rm m}}, \tag{7}$$

$$D = K_{\rm s}\left[1 + \phi(K_{\rm s}K_{\rm f}^{-1} - 1)\right], \tag{8}$$

$$\alpha = 1 - \frac{K_{\rm m}}{K_{\rm s}}, \tag{9}$$

where $K_{\rm m}$, $K_{\rm s}$ and $K_{\rm f}$ are the bulk moduli of the drained matrix as well as the solid and fluid phases, respectively, ϕ is the porosity, and $\mu_{\rm m}$ is the shear modulus of the drained matrix.

(ii) Biot–Euler equations

$$\tau_{xx,x} + \tau_{xz,z} = \rho v_{x,t} + \rho_{f2} q_{x,t} - f_x, \tag{10}$$

$$\tau_{xz,x} + \tau_{zz,z} = \rho v_{z,t} + \rho_{f2} q_{z,t} - f_z, \tag{11}$$

where

$$\rho = (1 - \phi)\rho_{\rm s} + \phi\rho_{f2}$$

is the composite density with $\rho_{\rm s}$ and ρ_{f2} denoting the solid and fluid densities, respectively, and f_x and f_z are body forces per unit volume in the x and z directions.

(iii) Darcy–Euler equations

$$-p_{2,x} = \rho_{f2} v_{x,t} + m q_{x,t} + \frac{\eta}{\kappa} q_x - g_x, \tag{12}$$

$$-p_{2,z} = \rho_{f2} v_{z,t} + m q_{z,t} + \frac{\eta}{\kappa} q_z - g_z, \tag{13}$$

where g_x and g_z are forces per unit volume that act on pore pressure, $m = \mathcal{T}\rho_{f2}/\phi$, with $\mathcal{T}$ denoting the tortuosity, η is the fluid viscosity and κ is the permeability of the medium. The source terms f_x, f_z, g_x, and g_z are spatial derivatives of the applied forces.

2.2 Equations of motion of a fluid

The equations of motion of a fluid of density ρ_{f1} and bulk modulus K are given by the stress–strain relation

$$-p_{1,t} = K(w_{x,x} + w_{z,z}) - s_{f1}, \tag{14}$$

and Euler's equations

$$-p_{1,x} = \rho_{f1} w_{x,t} - g_x, \quad -p_{1,z} = \rho_{f1} w_{z,t} - g_z, \tag{15}$$

where p_1 and w denote the fluid pressure and particle velocity, respectively.

3 ALGORITHM

Pseudospectral methods are an efficient and highly accurate technique for full-waveform modelling (Boyd 2001; Carcione 2007). The calculation of synthetic seismograms by using pseudospectral differential operators and in the presence of a free surface was first introduced by Kosloff *et al.* (1984), who considered an elastic medium and modelled the free surface by the so-called 'zero-padding' method. This approach requires one to include a wide zone with zero *P*- and *S*-wave velocities above the free surface of the model to circumvent the periodic boundary conditions distinct to the Fourier method. However, the performance of the zero-padding method to model surface waves is not optimal, mainly when sources and/or receivers are located near the surface. To overcome this problem, Kosloff *et al.* (1990) and Tessmer (1995) used the Chebyshev method to compute the derivatives along the vertical direction to solve the isotropic and anisotropic elastic wave equations, respectively. Unlike the Fourier method, the Chebyshev method is not periodic and allows for the incorporation of boundary conditions by using characteristic variables, in particular, free-surface conditions at the surface and non-reflecting conditions at the bottom of the mesh. The same approach is used to model wave propagation across a fluid/porous medium interface.

The presence of the diffusive slow wave makes Biot's differential equations stiff as they involve two vastly different timescales (Jain 1984), which poses a serious problem of stability or performance to a numerical solution. To overcome this problem, the differential equations are solved with the splitting algorithm introduced by Carcione & Quiroga-Goode (1995) for poro-acoustic media, and used by Carcione & Helle (1999) for poro-elastic media. The numerical solution of the regular, non-stiff part of the differential equations is obtained by using a fourth-order Runge–Kutta method as a time-stepping algorithm, the Chebyshev differential operator to compute the spatial derivatives along the vertical direction, and the Fourier differential operator along the horizontal direction. The Fourier and Chebyshev methods consist of a spatial discretization and calculation of spatial derivatives using the fast Fourier transform (Boyd 2001; Carcione 2007). The Fourier method is a collocation technique in which a continuous function is approximated by a truncated series of trigonometric functions, wherein the spectral expansion coefficients are chosen such that the approximate solution coincides with the exact solution at the discrete set of sampling or collocation points. The collocation points are defined by equidistant sampling points. Since the expansion functions are periodic, the Fourier method is appropriate for problems with periodic boundary conditions. In the Chebyshev method, the collocation points are the roots of the Chebyshev polynomials. It is appropriate for simulating Neumann and Dirichlet boundary conditions. The Fourier and Chebyshev methods are infinitely accurate up to the maximum wavenumber, or minimum wavelength, supported by the grid, which corresponds to a spatial wavelength of two gridpoints at the maximum grid spacing for the Chebyshev operator.

The conventional Chebyshev method has two major disadvantages. In the first place, the gridpoints are restricted to the Gauss–Lobatto collocation points. This poses a limitation regarding the location of the interfaces. Secondly, the clustering of gridpoints at the ends of the mesh restricts the time step of the time integration scheme, which has to be of the order $O(N^{-2})$ where N is the number of gridpoints. Here, we use a mapping transformation for the vertical coordinate which circumvents the severe stability condition of the integration method and distributes the gridpoints at arbitrary locations. By stretching the mesh, we increase the minimum grid spacing and hence are able to increase the time step of the Runge–Kutta algorithm, thus reducing the computation time. For this purpose we have implemented the stretching function and algorithm described by Kosloff & Tal-Ezer (1993), who claim to obtain time steps of the order $O(N^{-1})$. This has been verified by Renaut & Fröhlich (1996) for the 2-D acoustic wave equation. Furthermore, this transformation can be used for spatial grid adaptation (Augenbaum 1989; Guillard *et al.* 1992; Bayliss *et al.* 1995), in the sense that the collocation points can be redistributed and properly concentrated in regions with steep velocity gradients, fine layering and complex interface geometries. Similar mapping transformations can be applied in the horizontal directions, where the Fourier differential operator is used (Carcione 1996b). As the Chebyshev collocation points are not evenly spaced, the time step depends on the smallest grid cell at the end of the mesh. In general, stability can be achieved with the conditions of at least two gridpoints per minimum wavelength demanded by the Fourier method. The temporal stability conditions are based on the Runge–Kutta method which is : $v\Delta t/\Delta z < threshold$, where v is the maximum wave velocity, Δt is the time step and Δz is the minimum grid spacing. We used $threshold = 2.79$, which is the result of a stability analysis for the Runge–Kutta time integration described in Jain (1984, pp. 50–52).

3.1 Characteristic variables

Boundary conditions are implemented by using a boundary treatment based on characteristic variables (Kosloff *et al.* 1990; Carcione 1991, 1992, 1994). This method has been proposed by Gottlieb *et al.* (1982). Bayliss *et al.* (1986) have modelled free-surface and non-reflecting boundary conditions using this method. The wave equation is decomposed into outgoing and incoming wave modes perpendicular to the free surface. The outgoing waves are determined by the solution inside the domain, while the incoming waves are calculated from the boundary conditions.

In order to model the fluid/porous medium system, we use two grids, one for the fluid and another for the porous medium. As before, the wavefield is decomposed into incoming and outgoing wave modes at the interface between the media. The inward propagating waves depend on the solution exterior to the subdomains and therefore are computed from the boundary conditions, while

the behaviour of the outward propagating waves is determined by the solution inside the subdomains.

Let us compute the characteristic vector for the porous medium and fluid, respectively. Here we assume that the interface is perpendicular to the z-axis, but the approach is also valid for inclinined interfaces. The regular part, that is $\eta = 0$, of the poro-elastic equations can be recast as

$$\mathbf{v}_{,t} = \mathbf{A}\mathbf{v}_{,x} + \mathbf{B}\mathbf{v}_{,z} + \mathbf{s}, \tag{16}$$

where

$$\mathbf{v} = [v_x, v_z, q_x, q_z, \tau_{xx}, \tau_{zz}, \tau_{xz}, -p_2]^\top, \tag{17}$$

$$\mathbf{s} = [\gamma_{11} f_x + \gamma_{12} g_x, \gamma_{11} f_z + \gamma_{12} g_z, \gamma_{22} g_x + \gamma_{12} f_x, \gamma_{22} g_z + \gamma_{12} f_z, s_{xx}, s_{zz}, s_{xz}, s_{f2}]^\top \tag{18}$$

$$\mathbf{A} = \begin{pmatrix} 0 & 0 & 0 & 0 & \gamma_{11} & 0 & 0 & \gamma_{12} \\ 0 & 0 & 0 & 0 & 0 & 0 & \gamma_{11} & 0 \\ 0 & 0 & 0 & 0 & \gamma_{12} & 0 & 0 & \gamma_{22} \\ 0 & 0 & 0 & 0 & 0 & 0 & \gamma_{12} & 0 \\ E_m + \alpha^2 M & 0 & \alpha M & 0 & 0 & 0 & 0 & 0 \\ E_m + \alpha^2 M - 2\mu_m & 0 & \alpha M & 0 & 0 & 0 & 0 & 0 \\ 0 & \mu_m & 0 & 0 & 0 & 0 & 0 & 0 \\ \alpha M & 0 & M & 0 & 0 & 0 & 0 & 0 \end{pmatrix}, \tag{19}$$

$$\mathbf{B} = \begin{pmatrix} 0 & 0 & 0 & 0 & 0 & 0 & \gamma_{11} & 0 \\ 0 & 0 & 0 & 0 & 0 & \gamma_{11} & 0 & \gamma_{12} \\ 0 & 0 & 0 & 0 & 0 & 0 & \gamma_{12} & 0 \\ 0 & 0 & 0 & 0 & 0 & \gamma_{12} & 0 & \gamma_{22} \\ 0 & E_m + \alpha^2 M - 2\mu_m & 0 & \alpha M & 0 & 0 & 0 & 0 \\ 0 & E_m + \alpha^2 M & 0 & \alpha M & 0 & 0 & 0 & 0 \\ \mu_m & 0 & 0 & 0 & 0 & 0 & 0 & 0 \\ 0 & \alpha M & 0 & M & 0 & 0 & 0 & 0 \end{pmatrix}, \tag{20}$$

$$\gamma_{11} = \frac{m}{m\rho - \rho_{f2}^2}, \quad \gamma_{12} = -\frac{\rho_{f2}}{m\rho - \rho_{f2}^2}, \quad \gamma_{22} = \frac{\rho}{m\rho - \rho_{f2}^2}. \tag{21}$$

The source terms s are the temporal derivatives of the corresponding stresses or the pressure, respectively.

Consider the boundaries perpendicular to the z-direction. The characteristic vector is given by (Carcione 1991, 1994; Tessmer 1995)

$$\mathbf{c} = \mathbf{L}\mathbf{v}, \tag{22}$$

where $\mathbf{L}$ is the matrix whose rows are the left eigenvectors of matrix $\mathbf{B}$. Vector $\mathbf{c}$ satisfies

$$\mathbf{c}_{,t} = \mathbf{\Lambda}\mathbf{c}_{,z}, \tag{23}$$

where the diagonal matrix $\mathbf{\Lambda}$ is given by

$$\mathbf{\Lambda} = \mathbf{L}\mathbf{B}\mathbf{L}^{-1}. \tag{24}$$

The eigenvalues, that is, the elements of $\mathbf{\Lambda}$, are given by

$$0;\ \ 0;\ \ \pm V_\pm;\quad \pm\sqrt{\gamma_{11}\mu_m}, \qquad V_\pm = \sqrt{\frac{b \pm c}{2}}, \tag{25}$$

where

$$b = E_G\gamma_{11} + M(2\alpha\gamma_{12} + \gamma_{22}), \tag{26}$$

$$E_G = E_m + \alpha^2 M, \tag{27}$$

is the P wave Gassmann modulus (Carcione 2007), and c satisfies

$$b^2 - c^2 = 4E_m M(\gamma_{11}\gamma_{22} - \gamma_{12}^2) \quad (c > 0). \tag{28}$$

The non-zero eigenvalues are the velocities of the upgoing and downgoing waves. The third set of eigenvalues correspond to the fast P waves (plus-sign inside the square root) and slow P waves (minus-sign inside the square root); then follow the two eigenvalues corresponding to the upgoing and downgoing S waves. Matrix $\mathbf{L}$ is given by

$$\mathbf{L} = \begin{pmatrix} 0 & 0 & 0 & 0 & 1 & l_{16} & 0 & l_{18} \\ l_{21} & 0 & 1 & 0 & 0 & 0 & 0 & 0 \\ 0 & l_{32} & 0 & l_{34} & 0 & l_{36} & 0 & l_{38} \\ 0 & -l_{32} & 0 & -l_{34} & 0 & l_{36} & 0 & l_{38} \\ 0 & l_{52} & 0 & l_{54} & 0 & -l_{36} & 0 & l_{58} \\ 0 & -l_{52} & 0 & -l_{54} & 0 & -l_{36} & 0 & l_{58} \\ l_{71} & 0 & 0 & 0 & 0 & 0 & 1/2 & 0 \\ -l_{71} & 0 & 0 & 0 & 0 & 0 & 1/2 & 0 \end{pmatrix}, \tag{29}$$

where

$$l_{21} = -\frac{\gamma_{12}}{\gamma_{11}}, \quad l_{71} = -\frac{1}{2}\sqrt{\frac{\mu_m}{\gamma_{11}}}, \tag{30}$$

$$l_{16} = \frac{2\mu_m}{E_m} - 1, \quad l_{18} = -\frac{2\alpha\mu_m}{E_m}, \tag{31}$$

$$l_{32} = \left(\frac{M}{4cV_-}\right)[eE_G + \alpha(M\gamma_{22} - c)], \tag{32}$$

$$l_{52} = -\left(\frac{M}{4cV_+}\right)[eE_G + \alpha(M\gamma_{22} + c)], \tag{33}$$

$$l_{34} = -\left(\frac{M}{4fV_-}\right)[f + (E_m\gamma_{11} - Mg)c], \tag{34}$$

$$l_{54} = -\left(\frac{M}{4fV_+}\right)[f - (E_m\gamma_{11} - Mg)c], \tag{35}$$

$$l_{36} = -\frac{(\alpha\gamma_{11} + \gamma_{12})M}{2c}, \tag{36}$$

$$l_{38} = \frac{E_G\gamma_{11} - M\gamma_{22} + c}{4c}, \tag{37}$$

$$l_{58} = \frac{-E_G\gamma_{11} + M\gamma_{22} + c}{4c}, \tag{38}$$

with

$$\begin{aligned} e &= \alpha\gamma_{11} + 2\gamma_{12}, \\ f &= E_m^2\gamma_{11}^2 + 2E_m M\left[\alpha\gamma_{11}(\alpha e - \gamma_{22}) + 2\gamma_{12}^2\right] + M^2 g^2, \\ g &= \alpha e + \gamma_{22}. \end{aligned} \tag{39}$$

Note that $b = E_{\rm m}\gamma_{11} + Mg$. Hence, the characteristic vector (22) is given by

$$\mathbf{c} = \begin{pmatrix} c_1 \\ c_2 \\ c_3 \\ c_4 \\ c_5 \\ c_6 \\ c_7 \\ c_8 \end{pmatrix} = \begin{pmatrix} \tau_{xx} + l_{16}\tau_{zz} - l_{18}p_2 \\ l_{21}v_x + q_x \\ l_{32}v_z + l_{34}q_z + l_{36}\tau_{zz} - l_{38}p_2 \\ -l_{32}v_z - l_{34}q_z + l_{36}\tau_{zz} - l_{38}p_2 \\ l_{52}v_z + l_{54}q_z - l_{36}\tau_{zz} - l_{58}p_2 \\ -l_{52}v_z - l_{54}q_z - l_{36}\tau_{zz} - l_{58}p_2 \\ l_{71}v_x + \tau_{xz}/2 \\ -l_{71}v_x + \tau_{xz}/2 \end{pmatrix}. \tag{40}$$

It can be shown that the first two rows are the zero-eigenvalue characteristics, the third and fourth rows correspond to the slow P waves, the fifth and sixth rows to the fast P waves, and the seventh and eight rows to the up- and downgoing S waves, respectively. Consider now the same approach for the fluid, whose equations of motion are given by eqs (14) and (15). It is easy to show that the characteristic vector corresponding to the unknown vector $[w_x, w_z, -p_1]^\top$ and matrix

$$\mathbf{B} = \begin{pmatrix} 0 & 0 & 0 \\ 0 & 0 & \rho_{f1}^{-1} \\ 0 & K & 0 \end{pmatrix} \tag{41}$$

is

$$\mathbf{d} = \begin{pmatrix} d_1 \\ d_2 \\ d_3 \end{pmatrix} = \begin{pmatrix} w_x \\ -p_1 + I_{\rm f} w_z \\ -p_1 - I_{\rm f} w_z \end{pmatrix}, \tag{42}$$

where $I_{\rm f} = \sqrt{\rho_{f1} K}$ is the fluid impedance. The downgoing and upgoing characteristics are d_2 and d_3, respectively.

Assume that the porous medium is represented in the lower grid and consider the upper boundary. The characteristics describing waves travelling towards the upper boundary are the third, fifth and seventh elements of vector **c** defined in eq. (40). These characteristics and the zero characteristics corresponding to the first two elements should remain unchanged after the boundary treatment. The characteristics together with the boundary conditions lead to the boundary equations that are described in Appendices A, B and C.

4 SIMULATIONS

In the following, we illustrate the validity and accuracy of the algorithm and the boundary conditions by comparing the numerical and analytical solutions. We validate the splitting mechanism addressing the stiff part of Biot's equations by comparing the numerical solution to an analytical solution accounting for a viscous pore fluid. We also investigate the effects of a viscous pore fluid on an interface between a fluid and a porous medium, which is not amenable to an analytical treatment. Viscosity is causing attenuation and in combination with patchy fluid saturation is believed to be a major cause of seismic wave attenuation in the Earth (Santos *et al.* 2005; Rubino *et al.* 2009). Finally, we present numerical simulations for a heterogeneous model characterized by fractal distributions of the elastic and hydraulic parameters.

In the first experiment, we use the original model setup and material parameters of Feng & Johnson (1983a,b), who theoretically predicted an additional third surface wave for the sealed pore case that they called the 'true' surface wave. This surface wave mode is the surface wave equivalent to the slow P wave and can only be observed in porous media. The other two surface waves are the Rayleigh wave (Landau & Lifshitz 1986) with a velocity slightly higher than the fluid bulk wave velocity that is attenuated by 'leaking' energy into the fluid and the Stoneley or Scholte wave (Stoneley 1924; Scholte 1947) that becomes a pseudo-Stoneley wave in the porous case as it is leaking energy into the slow compressional wave.

The model consists of saturated sintered glass beads overlain by a fluid. Source and receiver are in the fluid domain slightly above the interface between the two media. The analytical results have been obtained with the recently published algorithm developed by Diaz & Ezziani (2010). This algorithm, which is based on the Cagniard-de Hoop technique used by Feng & Johnson (1983a,b), is also capable of determining the Green's functions and the responses for receivers situated in the porous medium.

In the first two examples, the size of the model is 386.25 × 360 mm. In the vertical direction the upper half is occupied by the fluid and the lower half by the porous medium, each with a mesh size of 309 × 81 gridpoints. The time step is 0.1 μs and we apply the source on the fluid pressure $p_{\rm f}$ with a time history defined by a Ricker-type wavelet

$$s(t) = \cos[2\pi f_0(t - t_0)] \cdot \exp[-2f_0^2(t - t_0)^2], \tag{43}$$

where t is the time, f_0 is the centre frequency and $t_0 = 1.5/f_0$ is half the length of the wavelet. We used $f_0 = 103.65$ kHz. The corresponding wavelet and its corresponding power spectrum are shown in Fig. 1. The medium parameters for the sintered glass beads and the saturating fluid are given in Table 1. The overlying fluid in the upper half-space has the same properties as the pore fluid saturating the underlying glass beads.

First, we consider the open-pore boundary conditions described in Appendix B1, where the fluid in the pores is connected with the overlying fluid layer. Fig. 2(a) shows a snapshot of the experiment after 80 μs. The asterisk indicates the source position and the triangles the positions of the receivers. The corresponding recordings are shown in Fig. 3. The horizontal distance between the source and the receiver is 0.1 m. The receiver in the fluid measures the pressure 5.32 mm above the interface while the receiver in the solid records the vertical displacements 3.31 mm below the interface. The receiver in the fluid shows the refracted P wave at ∼50 μs and the direct P wave in the fluid at ∼70 μs. The receiver in the solid records the fast P wave at ∼50 μs and the S wave at ∼80 μs. The pseudo-Stoneley wave which is very pronounced at ∼90 μs is leaking energy into the fluid phase and can therefore be detected on the fluid receiver as well.

Figs 2(b) and 4 show the same situation, but for sealed-pore boundary conditions. The head wave and the S wave have the same amplitude as in the case of the open-pore boundary conditions, which is not immediately obvious, as the traces are normalized. The pseudo-Stoneley wave is of much smaller amplitude and, in contrast to the open-pore boundary conditions, the receiver in the porous medium also records the 'true' surface wave at ∼130 μs. This surface wave does not transmit energy to the fluid or solid medium and its amplitude decays exponentially away from the interface. The amplitude decay is larger in the fluid than it is in the solid and therefore this phase is barely visible for the receiver located in the fluid. Note that in this experiment, the receiver is very close to the interface and the analytical solution involves a number of internal numerical routines, which causes its accuracy, particularly with regard to the slow P wave, to diminish in the immediate

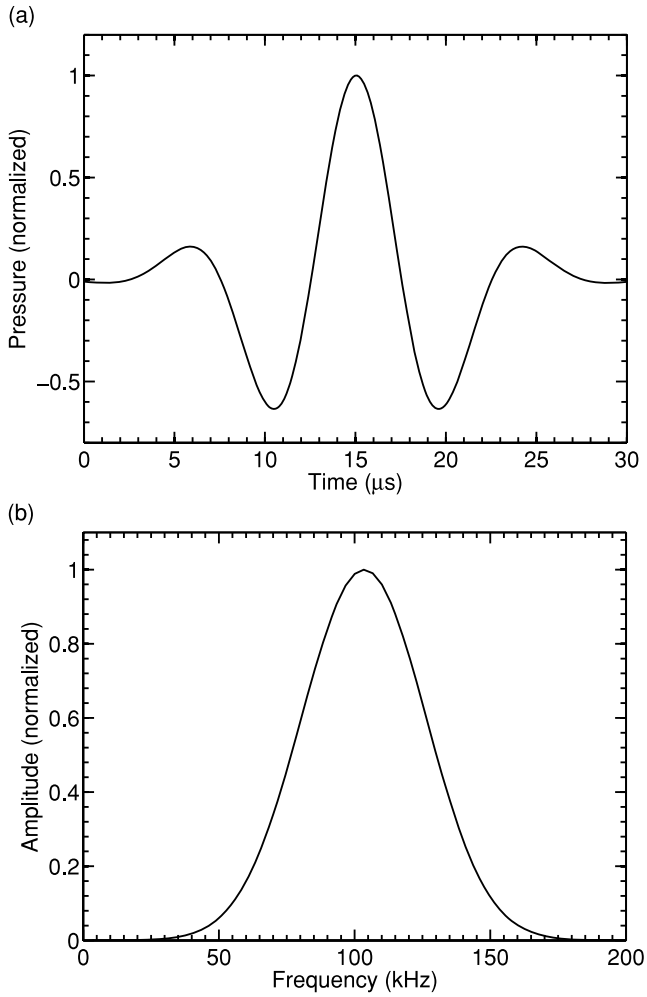

Figure 1. (a) Time-history and (b) power spectrum of the source wavelet used for the simulations shown in Figs 2, 3, 4 and 6.

Table 1. Poro-elastic properties of sintered glass beads.

Grain	Bulk modulus, K_s	49.9 GPa
	Shear modulus, μ_s	27.8 GPa
	Density, ρ_s	2480 kg m^{-3}
Matrix	Bulk modulus, K_m	6.1 GPa
	Shear modulus, μ_m	3.4 GPa
	Porosity, ϕ	0.38
	Permeability, κ	100 D
	Tortuosity, T	1.79
Fluid	Density, ρ_f	1000 kg m^{-3}
	Viscosity, η	0/0.1 Pa s
	Bulk modulus, K	2.25 GPa

vicinity of interfaces (Diaz & Ezziani 2010). Conversely, one observes a systematic and rapid convergence of the analytical and numerical solutions with increasing distance from the interface.

To test the validity of the splitting algorithm in the presence of a viscous pore fluid we compare our numerical solution to an analytical poro-acoustic solution based on Carcione & Quiroga-Goode (1995) that we apply to the poro-elastic case in the same way as de la Puente *et al.* (2008). The properties of the medium are described in Table 2 and the modelling domain with a dimension of 3000 × 3000 m consists of 121 × 122 nodes in horizontal and vertical directions, respectively. We use a explosive source with the time history of a Ricker wavelet characterized by a central

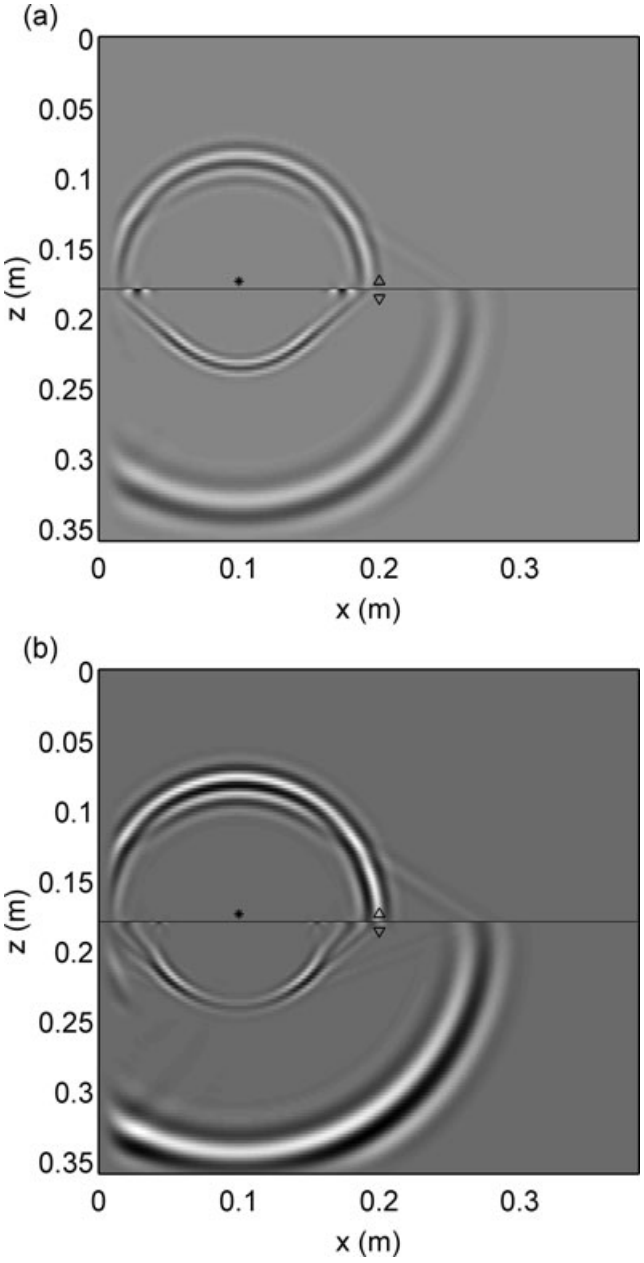

Figure 2. Snapshots of the fluid pressure at 80 μs propagation time for (a) open-pore and (b) closed-pore boundary conditions. The asterisk denotes the source location and the triangles correspond to the receiver locations. The medium parameters are given in Table 1.

frequency of 4.5 Hz and a time delay of 6.66×10^{-4} s that acts on the frame only, that is on all τ_{ij} with $i = j$. The receiver is placed at a distance of 500 m and records the fluid pressure. Fig. 5(a) shows the recordings for a non-viscous pore fluid and Fig. 5(b) shows the corresponding recording for a pore fluid with a viscosity of 0.001 Pa s. We see that there is excellent agreement between the analytical and numerical solutions for both non-viscous (Fig. 5a) and viscous (Fig. 5b) pore fluids.

Fig. 6 compares the results already shown in Figs 3 and 4 to the case of non-zero viscosity ($\eta = 0.1$ Pa s). Here, the fast P wave and the S wave are only slightly affected by attenuation. The Stoneley wave in turn experiences a significant amplitude drop that is clearly visible in the open-pore case (Figs 6a and d). As the amplitude of the Stoneley wave is small in the sealed pore case,

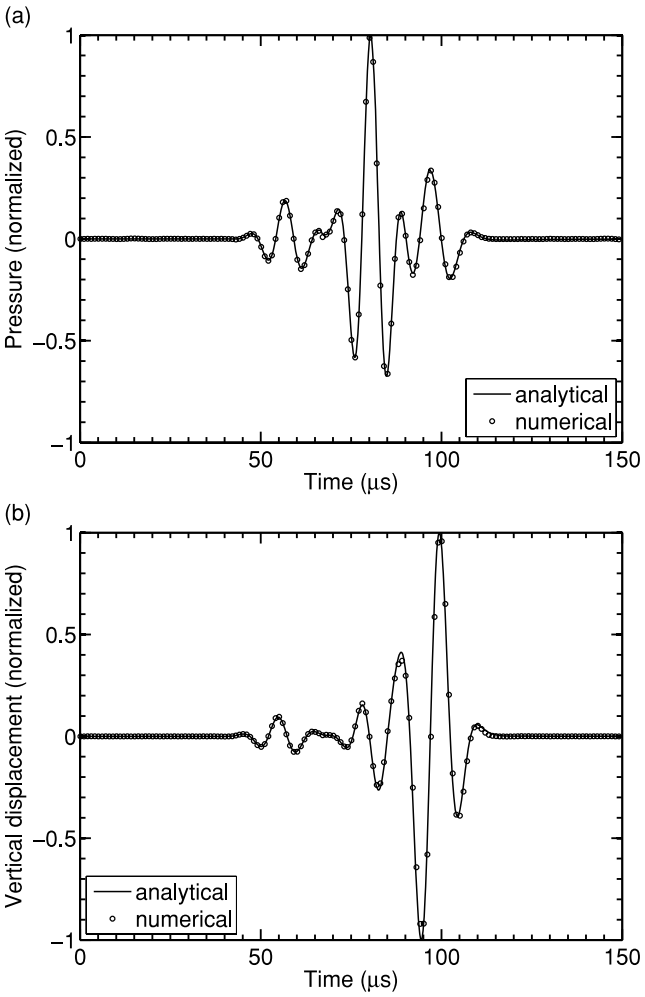

Figure 3. Comparison between the analytical (solid line) and numerical (dots) solutions for the open-pore boundary conditions (a) above and (b) below the interface. The receiver locations correspond to those shown in Fig. 2.

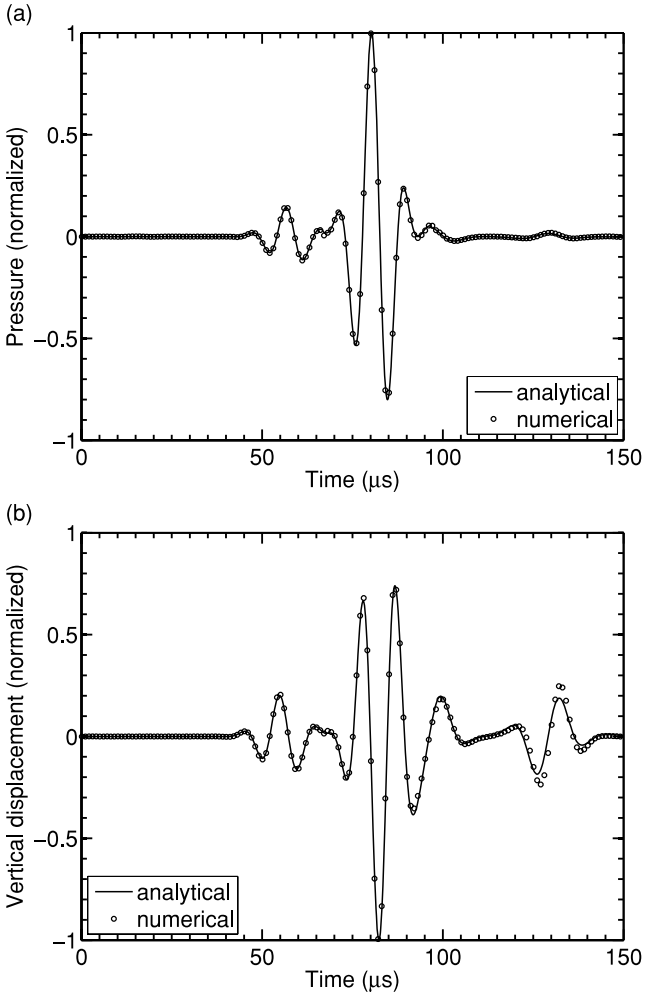

Figure 4. Same as Fig. 3, but for sealed-pore boundary conditions. Please note that, due to imbedded numerical approximations, the evaluation of seismograms close to the interface is also a challenge for the analytical solution, which may have contributed to the slight discrepancy between the analytical and numerical solutions for the true surface wave.

Table 2. Poro-elastic properties used for the test of the splitting scheme.

Grain	Bulk modulus, K_s	40.0 GPa
	Density, ρ_s	2500 kg m^{-3}
Matrix	Bulk modulus, K_m	32 GPa
	Porosity, ϕ	0.2
	Permeability, κ	600 mD
	Tortuosity, T	3
Fluid	Density, ρ_f	1040 kg m^{-3}
	Viscosity, η	0/0.001 Pa s
	Bulk modulus, K	2.5 GPa

its attenuation is rather marginal and can hardly be noticed on the fluid receiver (Fig. 6b). The true surface wave, which is even more strongly attenuated in the presence of viscosity is no longer observable at the considered source–receiver distance.

The next experiment considers a source–receiver distance of 750 m and a omni-directional fluid-pressure source with a centre frequency of 10 Hz. The parameters for the porous solid are given in Table 3 and correspond to a sandy seabed formation based on measurements by Williams *et al.* (2002). We use two grids consisting of 1001 × 160 nodes with a horizontal grid spacing of 2.5 m and layer thicknesses of 900 and 1000 m for the fluid and porous solid parts of the model, respectively. The source is located 17.9 m above the interface at a distance of 750 m from the left-hand border. The receiver is buried 0.6 m below the interface in the porous medium at a distance of 1500 m from the left-hand border of the model. The time step is 0.2 ms. Fig. 7(a) compares the vertical displacement to the analytical solution for a homogeneous porous medium saturated by a non-viscous pore fluid. The receiver records the fast P wave that is closely followed by the fluid wave, the S wave and the true surface wave. The same experiment for a viscous pore fluid is shown in Fig. 7(b). Due to the unavailability of an analytical solution, we compare the results to those of the corresponding non-viscous case (Fig. 7a). We see that the fast P wave and the fluid wave do not change, but that the S wave is not discernible due to the closely following Stoneley wave that replaces the true surface wave.

A fundamental advantage of numerical algorithms is the possibility to model wave propagation in strongly heterogeneous media. Indeed there is increasing evidence to suggest that seismic heterogeneities seem to be governed by remarkably uniform fractal scaling laws (Holliger & Goff 2003; Belina *et al.* 2009). To explore the implications for our case, we replace the homogeneous porosity distribution with a 2-D band-limited fractal distribution characterized by a von Kármán autocovariance function and a lognormal

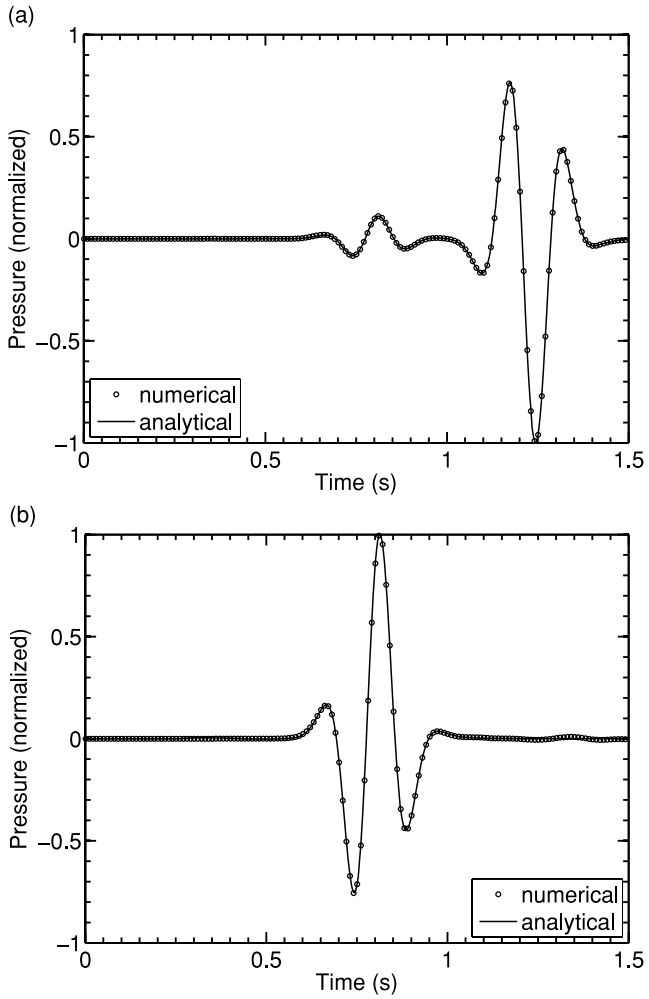

Figure 5. Comparison between the numerical (dots) and analytical (solid line) solutions for a (a) non-viscous pore fluid and (b) a pore fluid with a viscosity of 0.001 Pa s demonstrating that the splitting algorithm converges to the correct solution also in the presence of a viscous pore fluid. The receiver is located at a distance of 500 m from the solid pressure source, which has the time history of a Ricker wavelet with a central frequency of 4.5 Hz. The model parameters are given in Table 2.

probability density function (Sidler & Holliger 2010) with mean 0.385, variance of 0.01, $\nu = 0.2$, and horizontal and vertical correlation lengths of 1500 and 600 m. The parameter ν is related to the so-called Hausdorff fractal dimension *HD* and thus to the complexity of the medium as $HD = ED + 1 - \nu$ (e.g. Goff & Jordan 1988), where *ED* denotes the underlying Euclidean dimension of the stochastic process. In 2-D space, $\nu = 0$ thus corresponds to a highly complex space-filling surface, whereas $\nu = 1$ characterizes a very smooth surface. For $\nu = 0.5$ the von Kármán autocovariance function is equivalent to the widely used exponential autocovariance model. The corresponding porosity distribution is shown in Fig. 8(a). Based on this porosity distribution we calculate the permeability, tortuosity, shear modulus, and drained bulk modulus for each gridpoint using the empirical relationships described below. To obtain the permeability κ we use the Kozeny-Carman equation (Mavko *et al.* 1998)

$$\kappa = \frac{B\phi^3 d^2}{(1-\phi)^2}, \tag{44}$$

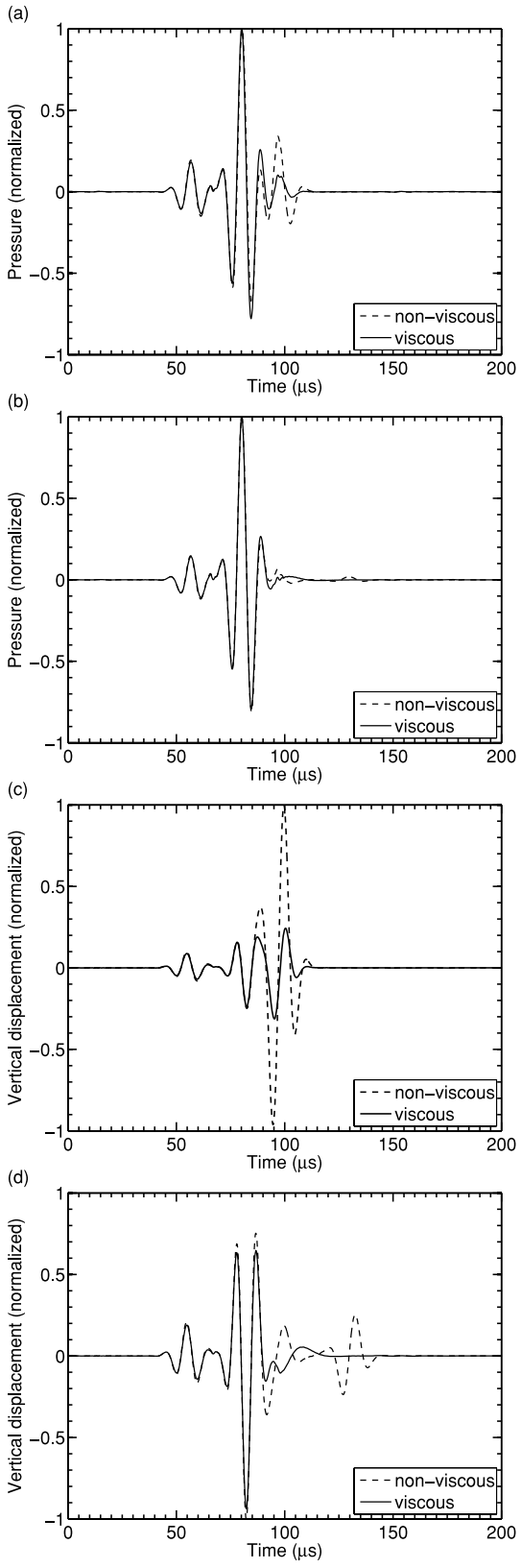

Figure 6. (a and b) Pressure response 5.32 mm above the interface and (c and d) vertical displacement 3.31 mm below the interface for (a and c) the open-pore and (b and d) the sealed-pore case, respectively. The solid line corresponds to a viscous pore fluid and the dashed line to an non-viscous pore fluid.

Table 3. Poro-elastic properties of unconsolidated sand.

Grain	Bulk modulus, K_s	32 GPa
	Shear modulus, μ_s	44 GPa
	Density, ρ_s	2690 kg m^{-3}
Matrix	Bulk modulus, K_m	1.36 GPa
	Shear modulus, μ_m	1.86 GPa
	Porosity, ϕ	0.38
	Permeability, κ	28.3 D
	Tortuosity, T	1.8
Fluid	Density, ρ_f	1000 kg m^{-3}
	Viscosity, η	0/0.00105 Pa s
	Bulk modulus, K	2.25 GPa

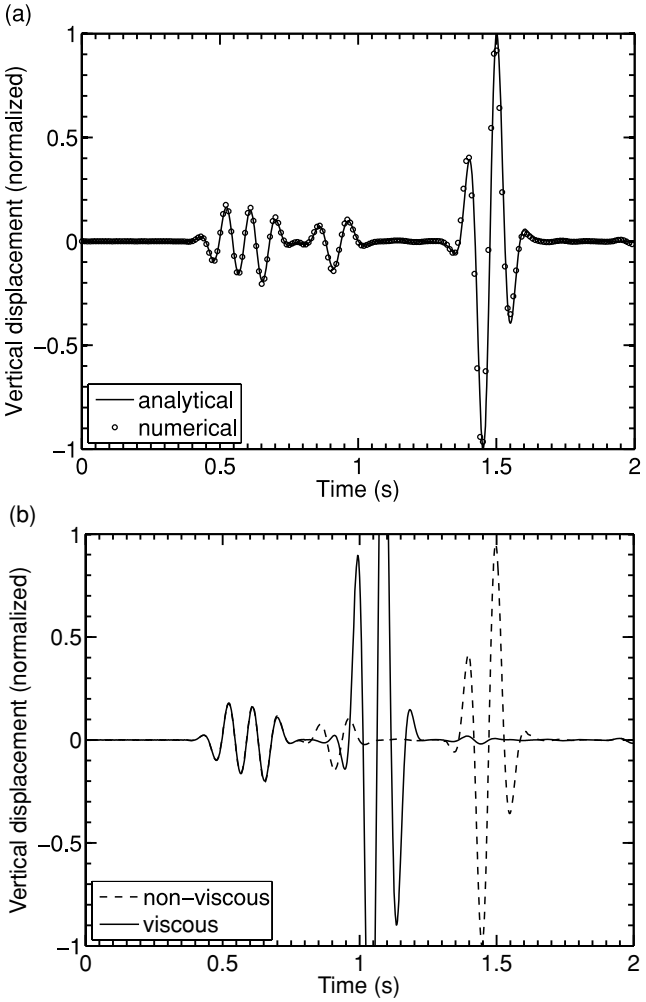

Figure 7. Numerical simulations of the vertical displacement recorded at a receiver located 0.6 m below the interface. (a) Homogeneous porous medium saturated by a non-viscous fluid compared to the analytical solution based on the Cagniard-de Hoop method; (b) homogeneous porous medium saturated by a viscous pore fluid compared to the solution given in (a). The model parameters are given in Table 3.

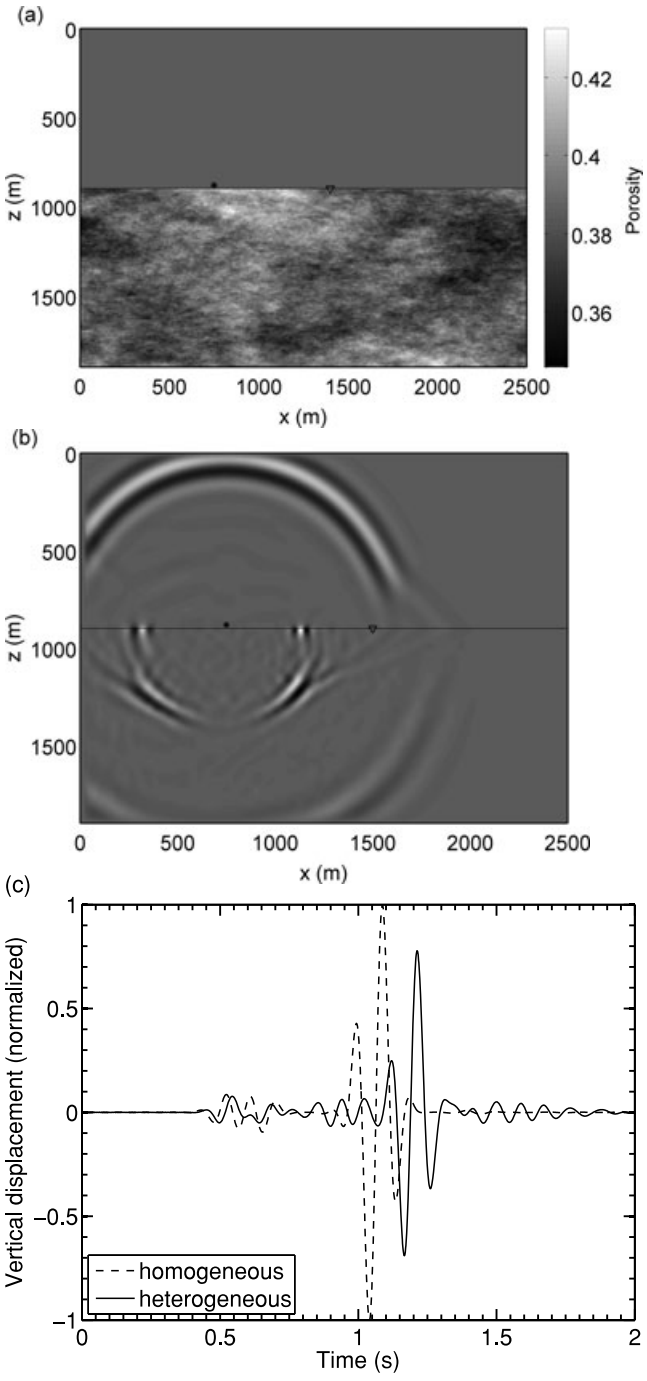

Figure 8. (a) Heterogeneous model based on a fractal porosity distribution. The asterisk denotes the source location and the triangle the receiver position. (b) Snapshot of the pore pressure after a propagation time of 0.72 s. (c) Seismic response recorded at the receiver location for a viscous pore fluid compared to the seismogram for the equivalent homogeneous model shown in Fig. 7(b).

where ϕ is the porosity, d is the grain diameter and $B = 0.003$. Jackson & Richardson (2007) specify an average grain diameter $d = 0.25$ mm for fine to medium sand. For the matrix and shear bulk moduli we use the Krief equations (Garat *et al.* 1990)

$$K_m = K_s(1-\phi)^{4/(1-\phi)}, \tag{45}$$

$$\mu_m = K_m \mu_s / K_s. \tag{46}$$

The tortuosity is evaluated as (Berryman 1980)

$$\mathcal{T} = \frac{1}{2}\left(1 + \frac{1}{\phi}\right). \tag{47}$$

Fig. 8(b) shows a snapshot of the fluid pressure after a propagation time of 0.72 s and Fig. 8(c) shows the vertical displacement at the receiver for the fractal model compared to the response of an equivalent homogeneous model. We see that in heterogeneous

models the *P* wave is delayed compared to the homogeneous case and that the Stoneley wave is considerably attenuated and delayed. The late arrival time of the Stoneley wave allows the *S* wave to be recognized. This is due to the combination of the low velocity zone of the fractal medium situated between the source and the receiver and the increased attenuation effects related to the fractal distribution of the elastic and hydraulic model parameters.

5 CONCLUSIONS

We have developed a pseudospectral numerical algorithm to simulate seismic wave propagation in porous media. The algorithm allows for an explicit treatment of interfaces and thus is particularly suitable for the accurate simulation of surface waves. Periodic Fourier operators with absorbing boundary conditions and non-periodic operators based on the Chebyshev expansion with explicit boundary treatment are applied in the horizontal and vertical directions, respectively. We use separate domains for each medium and decompose the wavefield at the boundary using a characteristics approach for an accurate treatment of wave propagation at the interface between the fluid and the porous medium. We consider the two extreme cases of open-pore and sealed-pore boundary conditions at the interface between a fluid and a porous medium. Free-surface and absorbing boundary conditions are applied at the top and bottom of the model, respectively. To verify and illustrate the accuracy of our method, we compare the numerical solutions to corresponding analytical solutions based on the Cagniard-de Hoop technique. Finally, we demonstrate the flexibility and versatility of our algorithm by applying it to models of porous media saturated by viscous fluids as well as strongly heterogeneous, fractal distributions of the poro-elastic material parameters.

ACKNOWLEDGMENTS

We are grateful to Julien Diaz for providing his code for the non-viscous analytical solutions and to Josep de la Puente for the Matlab program for the viscous analytical solution. We also wish to thank the editor Michael Korn as well as Stewart Greenhalgh and a second anonymous reviewer for their insightful and constructive comments that helped us to significantly improve the quality of this paper. This research has been supported in part by a grant from the Swiss National Science Foundation.

REFERENCES

Augenbaum, J.M., 1989. An adaptive pseudospectral method for discontinuous problems, *Appl. Numer. Math.,* **5,** 459–480.

Bayliss, A., Jordan, K.E., LeMesurier, B.J. & Turkel, E., 1986. A fourth-order accurate finite difference scheme for the computation of elastic waves, *Bull. seism. Soc. Am.,* **76,** 1115–1132.

Bayliss, A., Class, A. & Matkowsky, B.J., 1995. Adaptive approximation of solutions to problems with multiple layers by Chebyshev pseudo-spectral methods, *J. Comput. Phys.,* **116,** 160–172.

Belina, F.A., Ernst, J.R. & Holliger, K., 2009. Inversion of crosshole seismic data in heterogeneous environments: comparison of waveform and ray-based approaches, *J. appl. Geophys.,* **68,** 85–94.

Berryman, J.G., 1980. Confirmation of Biot's theory, *Appl. Phys. Lett.,* **37,** 382–384.

Biot, M.A., 1941. General theory of three-dimensional consolidation, *J. appl. Phys.,* **12,** 155–164.

Biot, M.A., 1956a. Theory of propagation of elastic waves in a fluid-saturated porous solid. I. Low-frequency range, *J. acoust. Soc. Am.,* **28,** 168–178.

Biot, M.A., 1956b. Theory of propagation of elastic waves in a fluid-saturated porous solid. II. Higher frequency range, *J. acoust. Soc. Am.,* **28,** 179–191.

Biot, M.A., 1962a. Mechanics of deformation and acoustic propagation in porous media, *J. Appl. Phys.,* **33,** 1482–1498.

Biot, M.A., 1962b. Generalized theory of acoustic propagation in porous dissipative media, *J. acoust. Soc. Am.,* **34,** 1254–1264.

Bourbié, T., Coussy, O. & Zinszner, B., 1987. *Acoustics of Porous Media*, Edition Technip, Paris.

Boyd, J.P., 2001. *Chebyshev and Fourier Spectral Methods*, 2nd edn, Dover Publications, New York.

Carcione, J.M., 1991. Domain decomposition for wave propagation problems, *J. Sci. Comput.,* **6,** 453–472.

Carcione, J.M., 1992. Modeling anelastic singular surface waves in the earth, *Geophysics,* **57,** 781–792.

Carcione, J.M., 1994. Time-dependent boundary conditions for the 2-D linear anisotropic-viscoelastic wave equation, *Numer. Methods Partial Different. Equat.,* **10,** 771–791.

Carcione, J.M., 1996a. Elastodynamics of a non-ideal interface: application to crack and fracture scattering, *J. geophys. Res.,* **101,** 28 177–28 188.

Carcione, J.M., 1996b. A 2-D Chebyshev differential operator for the elastic wave equation, *Comput. Method. Appl. M.,* **130,** 33–45.

Carcione, J.M., 1998. Viscoelastic effective rheologies for modeling wave propagation in porous media, *Geophys. Prospect.,* **46,** 249–270.

Carcione, J.M., 2007. *Wave Fields in Real Media: Wave Propagation in Anisotropic, Anelastic, Porous and Electromagnetic Media*, 2nd edn, Elsevier, Amsterdam.

Carcione, J.M. & Helle, H.B., 1999. Numerical solution of the poroviscoelastic wave equation on a staggered mesh, *J. Comput. Phys.,* **154,** 520–527.

Carcione, J.M. & Quiroga-Goode, G., 1995. Some aspects of the physics and numerical modeling of Biot compressional waves, *J. Comput. Acoust.,* **3,** 261–280.

Chandler, R.N., 1981. Transient streaming potential measurements on fluid-saturated porous structures: an experiment verification of Biot's slow wave in the quasi-static limit, *J. acoust. Soc. Am.,* **70,** 116–121.

de la Puente, J., Dumbser, M., Käser, M. & Igel, H., 2008. Discontinuous Galerkin methods for wave propagation in poroelastic media, *Geophysics,* **73,** T77–T97.

Deresiewicz, H., 1962. The effect of boundaries on wave propagation in a liquid-filled porous-solid, IV. Surface waves in a half-space, *Bull. seism. Soc. Am.,* **52,** 627–638.

Deresiewicz, H. & Rice, J.T., 1962. The effect of boundaries on wave propagation in a liquid-filled porous solid: III. Reflection of plane waves at a free plane boundary (general case), *Bull. seism. Soc. Am.,* **52,** 595–625.

Diaz, J. & Ezziani, A., 2010. Analytical solution for waves propagation in heterogeneous acoustic/porous media. Part I: the 2D case, *Commun. Comput. Phys.,* **7,** 171–194.

Edelman, I. & Wilmanski, K., 2002. Asymptotic analysis of surface waves at vacuum/porous medium and liquid/porous medium interfaces, *Continuum Mech. Therm.,* **14,** 25–44.

Feng, S. & Johnson, D.L., 1983a. High-frequency acoustic properties of a fluid/porous solid interface. I. New surface mode, *J. acoust. Soc. Am.,* **74,** 906–914.

Feng, S. & Johnson, D.L., 1983b. High-frequency acoustic properties of a fluid/porous solid interface. II. The 2D reflection Green's function, *J. acoust. Soc. Am.,* **74,** 915–924.

Garat, J., Krief, M., Stellingwerff, J. & Ventre, J., 1990. A petrophysical interpretation using the velocities of P and S waves (full waveform sonic), *Log Analyst,* **31,** 355–369.

Geerstma, J. & Smit, D.C., 1961. Some aspects of elastic wave propagation in fluid-saturated porous solids, *Geophysics,* **26,** 169–181.

Goff, J.A. & Jordan, T.H., 1988. Stochastic modeling of seafloor morphology: inversion of sea beam data for second-order statistics, *J. geophys. Res.,* **93,** 13 589–13 608.

Gottlieb, D., Gunzburger, M. & Turkel, E., 1982. On numerical boundary treatment of hyperbolic systems for finite difference and finite element methods, *SIAM J. Numer. Anal.,* **19,** 671–682.

Guillard, H., Malé, J.M. & Peyret, R., 1992. Adaptive spectral methods with application to mixing layer computations, *J. Comput. Phys.,* **102,** 114–127.

Hardy, H. & Beier, R.A., 1994. *Fractals in Reservoir Engineering*, World Scientific, Singapore.

Holland, C.W., 1991. Surface waves in poro-viscoelastic marine sediments, in *Shear Waves in Marine Sediments*, pp. 13–20, eds Hovem, J.M., Richardson, M.D. & Stoll, R.D., Kluwer, Dordrecht.

Holliger, K., 1996. Upper crustal seismic velocity heterogeneity as derived from a variety of P-wave sonic logs, *Geophys. J. Int.,* **125,** 813–829.

Holliger, K. & Goff, J.A., 2003. A generic model for the 1/f-scaling nature of seismic velocity fluctuations, in *Heterogenity in the Crust and Upper Mantle—Nature, Scaling and Seismic Properties*, pp. 131–154, eds Goff, J.A. & Holliger, K., Kluwer Academic, New York.

Jackson, D.R. & Richardson, M.D., 2007. *High-Frequency Seafloor Acoustics*, Springer, New York.

Jain, M.K., 1984. *Numerical Solutions of Differential Equations*, 2nd edn, Wiley Eastern, New Delhi.

Johnson, J.B., 1982. On the application of Biot's theory to acoustic wave propagation in snow, *Cold Reg. Sci. Technol.,* **6,** 49–60.

Kosloff, D. & Tal-Ezer, H., 1993. A modified Chebyshev pseudospectral method with an $O(N^{-1})$ time step restriction, *J. Comput. Phys.,* **104,** 457–469.

Kosloff, D., Reshef, M. & Loewenthal, D., 1984. Elastic wave calculations by the fourier method, *Bull. seism. Soc. Am.,* **74,** 875–891.

Kosloff, D., Kessler, D., Filho, A.Q., Tessmer, E., Behle, A. & Strahilevitz, R., 1990. Solution of the equations of dynamic elasticity by a Chebychev spectral method, *Geophysics,* **55,** 734–748.

Landau, L.D. & Lifshitz, E.M., 1986. *Theory of Elasticity*, 3rd edn, Elsevier, Amsterdam.

Mavko, G., Mukerji, T. & Dvorkin, J., 1998. *The Rock Physics Handbook: Tools for Seismic Analysis in Porous Media*, Cambridge University Press, Cambridge.

Mittet, R., 2002. Free-surface boundary conditions for elastic staggered-grid modeling schemes, *Geophysics,* **67,** 1616–1623.

Morency, C. & Tromp, J., 2008. Spectral-element simulation of wave propagation in porous media, *Geophys. J. Int.,* **175,** 301–345.

Nagy, P.B., 1992. Observation of a new surface mode on a fluid-saturated permeable solid, *Appl. Phys. Lett.,* **60,** 2735–2737.

Oura, H., 1952. Reflection of sound at snow surface and mechanism of sound propagation in snow, *Low Temp. Sci.,* **9,** 179–186.

Plona, T.J., 1980. Observation of a second bulk compressional wave in a porous medium at ultrasonic frequencies, *Appl. Phys. Lett.,* **36,** 259–261.

Renaut, R. & Fröhlich, J., 1996. A pseudospectral Chebychev method for the 2D wave equation with domain stretching and absorbing boundary conditions, *J. Comput. Phys.,* **124,** 324–336.

Rubino, J.G., Ravazzoli, C.L. & Santos, J.E., 2009. Equivalent viscoelastic solids for heterogeneous fluid-saturated porous rocks, *Geophysics,* **74,** N1–N13.

Santos, J.E., Ravazzoli, C.L., Gauzellino, P. & Carcione, J.M., 2005. Numerical simulation of ultrasonic waves in reservoir rocks with patchy saturation and fractal petrophysical properties, *Comput. Geosci.,* **9,** 1–27.

Scholte, J.G., 1947. On Rayleigh waves in visco-elastic media, *Physica,* **13,** 245–250.

Sidler, R. & Holliger, K., 2010. Seismic reflectivity of the sediment-covered seafloor: effects of velocity gradients and fine-scale layering, *Geophys. J. Int.,* **181,** 521–531.

Stoneley, R., 1924. Elastic waves at the surface of separation of two solids, in *Proc. R. Soc. Lond. A,* **106,** 416–428.

Terzaghi, K., 1923. Die Berechnung der Durchlässigkeitsziffer des Tones aus dem Verlauf der hydrodynamischen Spannungserscheinungen, *Sitzungsberichte der Akademie der Wissenschaften in Wien,* **132,** 125–138.

Terzaghi, K., 1943. *Theoretical Soil Mechanics*, John Wiley and Sons, New York.

Tessmer, E., 1995. 3-D seismic modelling of general anisotropy in the presence of the free surface by a Chebyshev spectral method, *Geophysics,* **121,** 557–575.

Turcotte, D.L., 1997. *Fractals and Chaos in Geology and Geophysics*, 2nd edn, Cambridge University Press, Cambridge.

Van der Grinten, J., Van Dongen, M.E.H. & Van der Kogel, H., 1985. A shock tube technique for studying pore pressure propagation in a dry and water-saturated porous medium, *J. appl. Phys.,* **58,** 2937–2942.

Williams, K.L., Jackson, D.R., Thorsos, E.I., Tang, D. & Schock, S.G., 2002. Comparison of sound speed and attenuation measured in a sandy sediment to predictions based on the Biot theory of porous media, *IEEE J. Ocean. Eng.,* **27,** 413–428.

APPENDIX A: FREE-SURFACE BOUNDARY CONDITIONS

The boundary conditions at the free surface of a porous medium are (Deresiewicz 1962; Carcione 2007)

$$\tau_{zz} = \tau_{xz} = 0, \quad p_2 = 0. \tag{A1}$$

Let the superscripts (old) and (new) denote values of variables before and after the application of the boundary conditions at the upper boundary of the mesh. Retaining the upward characteristics yields

$$\begin{aligned}
&\tau_{xx}^{(\mathrm{new})} = c_1^{(\mathrm{old})},\\
&l_{21} v_x^{(\mathrm{new})} + q_x^{(\mathrm{new})} = c_2^{(\mathrm{old})},\\
&l_{32} v_z^{(\mathrm{new})} + l_{34} q_z^{(\mathrm{new})} = c_3^{(\mathrm{old})},\\
&l_{52} v_z^{(\mathrm{new})} + l_{54} q_z^{(\mathrm{new})} = c_5^{(\mathrm{old})},\\
&l_{71} v_x^{(\mathrm{new})} = c_7^{(\mathrm{old})},
\end{aligned} \tag{A2}$$

where $c_J^{(\mathrm{old})}$, $J = 1, \ldots, 7$ are the old components of vector $\mathbf{c}$. Solving the system (A2) gives the boundary equations

$$\begin{aligned}
&v_x^{(\mathrm{new})} = c_7^{(\mathrm{old})}/l_{71},\\
&v_z^{(\mathrm{new})} = \left(l_{54} c_3^{(\mathrm{old})} - l_{34} c_5^{(\mathrm{old})}\right)/(l_{32} l_{54} - l_{34} l_{52}),\\
&q_x^{(\mathrm{new})} = c_2^{(\mathrm{old})} - c_7^{(\mathrm{old})}(l_{21}/l_{71}),\\
&q_z^{(\mathrm{new})} = \left(l_{32} c_5^{(\mathrm{old})} - l_{52} c_3^{(\mathrm{old})}\right)/(l_{32} l_{54} - l_{34} l_{52}),\\
&\tau_{xx}^{(\mathrm{new})} = c_1^{(\mathrm{old})},\\
&\tau_{zz}^{(\mathrm{new})} = 0,\\
&\tau_{xz}^{(\mathrm{new})} = 0,\\
&-p_2^{(\mathrm{new})} = 0.
\end{aligned} \tag{A3}$$

Similarly, the boundary equations for the lower boundary are

$$\begin{aligned}
&v_x^{(\mathrm{new})} = -c_8^{(\mathrm{old})}/l_{71},\\
&v_z^{(\mathrm{new})} = \left(l_{34} c_6^{(\mathrm{old})} - l_{54} c_4^{(\mathrm{old})}\right)/(l_{32} l_{54} - l_{34} l_{52}),\\
&q_x^{(\mathrm{new})} = c_2^{(\mathrm{old})} + c_8^{(\mathrm{old})}(l_{21}/l_{71}),\\
&q_z^{(\mathrm{new})} = \left(l_{52} c_4^{(\mathrm{old})} - l_{32} c_6^{(\mathrm{old})}\right)/(l_{32} l_{54} - l_{34} l_{52}),\\
&\tau_{xx}^{(\mathrm{new})} = c_1^{(\mathrm{old})},\\
&\tau_{zz}^{(\mathrm{new})} = 0,\\
&\tau_{xz}^{(\mathrm{new})} = 0,\\
&-p_2^{(\mathrm{new})} = 0.
\end{aligned} \tag{A4}$$

APPENDIX B: FLUID/POROUS-MEDIUM BOUNDARY CONDITIONS

The boundary conditions at an interface between a porous medium and a fluid are (Deresiewicz 1962; Deresiewicz & Rice 1962; Bourbié *et al.* 1987; Carcione 2007)

$$q_z + v_z = w_z, \quad p_2 - p_1 = Tq_z, \quad \tau_{zz} = -p_1, \quad \tau_{xz} = 0, \tag{B1}$$

where T is a surface flow impedance (Feng & Johnson 1983a,b). Two limiting cases that we shall consider in the following are the so-called open-pore and sealed-pore conditions.

B1 Open-pore interface

In this case $T = 0$ and there is free fluid flow across the interface. The corresponding boundary conditions are

$$q_z + v_z = w_z, \quad p_2 = p_1, \quad \tau_{zz} = -p_1, \quad \tau_{xz} = 0. \tag{B2}$$

The upgoing characteristics c_3, c_5, and c_7 of the porous medium and the downgoing characteristics d_2 of the fluid must remain unchanged by the boundary treatment. Also, the characteristics related to a zero eigenvalue should remain unchanged. These requirements and the boundary conditions generate a system of six linear equations with six unknowns for the z-components. The corresponding solution is given by

$$\begin{aligned}
&v_x^{(\mathrm{new})} = c_7^{(\mathrm{old})}/l_{71},\\
&Dv_z^{(\mathrm{new})} = c_5^{(\mathrm{old})}[l_{34} - I_{\mathrm{f}}(l_{36} + l_{38})] - c_3^{(\mathrm{old})}[l_{54} - I_{\mathrm{f}}(l_{58} - l_{36})]\\
&\qquad + d_2^{(\mathrm{old})} l_3,\\
&q_x^{(\mathrm{new})} = c_2^{(\mathrm{old})} - c_7^{(\mathrm{old})}(l_{21}/l_{71}),\\
&Dq_z^{(\mathrm{new})} = -c_5^{(\mathrm{old})}[l_{32} - I_{\mathrm{f}}(l_{36} + l_{38})] + c_3^{(\mathrm{old})}[l_{52} - I_{\mathrm{f}}(l_{58} - l_{36})]\\
&\qquad - d_2^{(\mathrm{old})} l_2,\\
&\tau_{xx}^{(\mathrm{new})} = c_1^{(\mathrm{old})} - (l_{16} + l_{18})\tau_{zz}^{(\mathrm{new})},\\
&D\tau_{zz}^{(\mathrm{new})} = c_5^{(\mathrm{old})} I_{\mathrm{f}}(l_{32} - l_{34}) + c_3^{(\mathrm{old})} I_{\mathrm{f}}(l_{54} - l_{52}) + d_2^{(\mathrm{old})} l_1,\\
&\tau_{xz}^{(\mathrm{new})} = 0,\\
&-p_2^{(\mathrm{new})} = \tau_{zz}^{(\mathrm{new})},\\
&w_x^{(\mathrm{new})} = w_x^{(\mathrm{old})},\\
&w_z^{(\mathrm{new})} = q_z^{(\mathrm{new})} + v_z^{(\mathrm{new})},\\
&p_1^{(\mathrm{new})} = p_2^{(\mathrm{new})},
\end{aligned} \tag{B3}$$

where

$$\begin{aligned}
&l_1 = l_{34}l_{52} - l_{32}l_{54},\\
&l_2 = (l_{36} + l_{38})l_{52} + (l_{36} - l_{58})l_{32},\\
&l_3 = (l_{36} + l_{38})l_{54} + (l_{36} - l_{58})l_{34},\\
&D = l_1 + I_{\mathrm{f}}(l_3 - l_2).
\end{aligned} \tag{B4}$$

Similarly, the boundary equations for the lower boundary are

$$\begin{aligned}
&v_x^{(\mathrm{new})} = -c_8^{(\mathrm{old})}/l_{71},\\
&Dv_z^{(\mathrm{new})} = -c_6^{(\mathrm{old})}[l_{34} - I_{\mathrm{f}}(l_{36} + l_{38})] + c_4^{(\mathrm{old})}[l_{54} - I_{\mathrm{f}}(l_{58} - l_{36})]\\
&\qquad - d_3^{(\mathrm{old})} l_3,\\
&q_x^{(\mathrm{new})} = c_2^{(\mathrm{old})} + c_8^{(\mathrm{old})}(l_{21}/l_{71}),\\
&Dq_z^{(\mathrm{new})} = c_6^{(\mathrm{old})}[l_{32} - I_{\mathrm{f}}(l_{36} + l_{38})] - c_4^{(\mathrm{old})}[l_{52} - I_{\mathrm{f}}(l_{58} - l_{36})]\\
&\qquad + d_3^{(\mathrm{old})} l_2,\\
&\tau_{xx}^{(\mathrm{new})} = c_1^{(\mathrm{old})} - (l_{16} + l_{18})\tau_{zz}^{(\mathrm{new})},\\
&D\tau_{zz}^{(\mathrm{new})} = c_6^{(\mathrm{old})} I_{\mathrm{f}}(l_{32} - l_{34}) + c_4^{(\mathrm{old})} I_{\mathrm{f}}(l_{54} - l_{52}) + d_3^{(\mathrm{old})} l_1,\\
&\tau_{xz}^{(\mathrm{new})} = 0,\\
&-p_2^{(\mathrm{new})} = \tau_{zz}^{(\mathrm{new})},\\
&w_x^{(\mathrm{new})} = w_x^{(\mathrm{old})},\\
&w_z^{(\mathrm{new})} = q_z^{(\mathrm{new})} + v_z^{(\mathrm{new})},\\
&p_1^{(\mathrm{new})} = p_2^{(\mathrm{new})}.
\end{aligned} \tag{B5}$$

B2 Sealed-pore interface

In this case we have $T = \infty$ and there is no relative flow across the interface. The boundary conditions are (Feng & Johnson 1983a,b; Carcione 2007)

$$v_z = w_z, \quad q_z = 0, \quad \tau_{zz} = -p_1, \quad \tau_{xz} = 0. \tag{B6}$$

In analogy with the open-pore interface, the combination of these boundary conditions and the requirements on the characteristic variables yields

$$\begin{aligned}
&v_x^{(\mathrm{new})} = c_7^{(\mathrm{old})}/l_{71},\\
&Dv_z^{(\mathrm{new})} = c_5^{(\mathrm{old})} l_{38} - c_3^{(\mathrm{old})} l_{58} + d_2^{(\mathrm{old})} l_{36}(l_{38} + l_{58})\\
&q_x^{(\mathrm{new})} = c_2^{(\mathrm{old})} - c_7^{(\mathrm{old})}(l_{21}/l_{71}),\\
&q_z^{(\mathrm{new})} = 0,\\
&D\tau_{zz}^{(\mathrm{new})} = I_{\mathrm{f}}\left(l_{58}c_3^{(\mathrm{old})} - l_{38}c_5^{(\mathrm{old})}\right) + d_2^{(\mathrm{old})}(l_{38}l_{52} - l_{32}l_{58})\\
&Dp_2^{(\mathrm{new})} = c_5^{(\mathrm{old})}(l_{32} - I_{\mathrm{f}}l_{36}) + d_2^{(\mathrm{old})} l_{36}(l_{32} + l_{52}) - c_3^{(\mathrm{old})}(I_{\mathrm{f}}l_{36} + l_{52})\\
&\tau_{xz}^{(\mathrm{new})} = 0,\\
&\tau_{xx}^{(\mathrm{new})} = c_1^{(\mathrm{old})} - l_{16}\tau_{zz}^{(\mathrm{new})} + l_{18}p_2^{(\mathrm{new})}\\
&w_x^{(\mathrm{new})} = w_x^{(\mathrm{old})}\\
&w_z^{(\mathrm{new})} = v_z^{(\mathrm{new})}\\
&-p_1^{(\mathrm{new})} = \tau_{zz}^{(\mathrm{new})},
\end{aligned} \tag{B7}$$

where

$$D = l_{52}l_{38} - l_{32}l_{58} + I_{\mathrm{f}}(l_{36}l_{38} + l_{36}l_{58}). \tag{B8}$$

Similarly, the boundary equations for the lower boundary are

$$\begin{aligned}
&v_x^{(\mathrm{new})} = -c_8^{(\mathrm{old})}/l_{71},\\
&Dv_z^{(\mathrm{new})} = -c_6^{(\mathrm{old})} l_{38} + c_4^{(\mathrm{old})} l_{58} - d_3^{(\mathrm{old})} l_{36}(l_{38} + l_{58}),\\
&q_x^{(\mathrm{new})} = c_2^{(\mathrm{old})} + c_8^{(\mathrm{old})}(l_{21}/l_{71}),\\
&q_z^{(\mathrm{new})} = 0,\\
&D\tau_{zz}^{(\mathrm{new})} = I_{\mathrm{f}}\left(l_{58}c_4^{(\mathrm{old})} - l_{38}c_6^{(\mathrm{old})}\right) + d_3^{(\mathrm{old})}(l_{38}l_{52} - l_{32}l_{58}),\\
&Dp_2^{(\mathrm{new})} = c_6^{(\mathrm{old})}(l_{32} - I_{\mathrm{f}}l_{36}) + d_3^{(\mathrm{old})} l_{36}(l_{32} + l_{52}) - c_4^{(\mathrm{old})}(I_{\mathrm{f}}l_{36} + l_{52}),\\
&\tau_{xz}^{(\mathrm{new})} = 0,\\
&\tau_{xx}^{(\mathrm{new})} = c_1^{(\mathrm{old})} - l_{16}\tau_{zz}^{(\mathrm{new})} + l_{18}p_2^{(\mathrm{new})},\\
&w_x^{(\mathrm{new})} = w_x^{(\mathrm{old})},\\
&w_z^{(\mathrm{new})} = v_z^{(\mathrm{new})},\\
&-p_1^{(\mathrm{new})} = \tau_{zz}^{(\mathrm{new})}.
\end{aligned} \tag{B9}$$

APPENDIX C: NON-REFLECTING BOUNDARY CONDITIONS

The non-reflecting or transparent boundary condition is achieved by keeping the characteristic variables describing outward motion unchanged and setting the characteristic variables, that describe motion into the grid to zero. Considering the bottom of the grid, the downgoing characteristics are c_4, c_6 and c_8, and we set c_3, c_5 and c_7 to zero. The resulting equations are

$$
\begin{aligned}
v_x^{(\mathrm{new})} &= -c_8^{(\mathrm{old})}/(2l_{71}),\\
2v_z^{(\mathrm{new})} &= \left(c_6^{(\mathrm{old})}l_{34} - c_4^{(\mathrm{old})}l_{54}\right)/(l_{32}l_{54} - l_{34}l_{52}),\\
q_x^{(\mathrm{new})} &= c_2^{(\mathrm{old})} + c_8^{(\mathrm{old})}(l_{21}/2l_{71}),\\
2q_z^{(\mathrm{new})} &= -\left(c_6^{(\mathrm{old})}l_{32} - c_4^{(\mathrm{old})}l_{52}\right)/(l_{32}l_{54} - l_{34}l_{52}),\\
-2p_2^{(\mathrm{new})} &= \left(c_4^{(\mathrm{old})} + c_6^{(\mathrm{old})}\right)/(l_{38} + l_{58}),\\
2\tau_{zz}^{(\mathrm{new})} &= \left(c_4^{(\mathrm{old})}l_{58} - c_6^{(\mathrm{old})}l_{38}\right)/[l_{36}(l_{38} + l_{58})],\\
\tau_{xx}^{(\mathrm{new})} &= c_1^{(\mathrm{old})} - l_{16}\tau_{zz}^{(\mathrm{new})} + l_{18}p_2^{(\mathrm{new})},\\
\tau_{xz}^{(\mathrm{new})} &= c_8^{(\mathrm{old})}.
\end{aligned}
\tag{C1}
$$

The non-reflecting boundary equations for the upper boundary are

$$
\begin{aligned}
v_x^{(\mathrm{new})} &= c_7^{(\mathrm{old})}/(2l_{71}),\\
2v_z^{(\mathrm{new})} &= \left(c_3^{(\mathrm{old})}l_{54} - c_5^{(\mathrm{old})}l_{34}\right)/(l_{32}l_{54} - l_{34}l_{52}),\\
q_x^{(\mathrm{new})} &= c_2^{(\mathrm{old})} - c_7^{(\mathrm{old})}(l_{21}/2l_{71}),\\
2q_z^{(\mathrm{new})} &= -\left(c_3^{(\mathrm{old})}l_{52} - c_5^{(\mathrm{old})}l_{32}\right)/(l_{32}l_{54} - l_{34}l_{52}),\\
-2p_2^{(\mathrm{new})} &= \left(c_3^{(\mathrm{old})} + c_5^{(\mathrm{old})}\right)/(l_{38} + l_{58}),\\
2\tau_{zz}^{(\mathrm{new})} &= \left(c_3^{(\mathrm{old})}l_{58} - c_5^{(\mathrm{old})}l_{38}\right)/[l_{36}(l_{38} + l_{58})],\\
\tau_{xx}^{(\mathrm{new})} &= c_1^{(\mathrm{old})} - l_{16}\tau_{zz}^{(\mathrm{new})} + l_{18}p_2^{(\mathrm{new})},\\
\tau_{xz}^{(\mathrm{new})} &= c_7^{(\mathrm{old})}.
\end{aligned}
\tag{C2}
$$

On the other hand, the equations at the lower boundary of the mesh representing the fluid are

$$
\begin{aligned}
w_x^{(\mathrm{new})} &= w_x^{(\mathrm{old})},\\
w_z^{(\mathrm{new})} &= d_2^{(\mathrm{old})}/(2I_{\mathrm{f}}),\\
-p_1^{(\mathrm{new})} &= d_2^{(\mathrm{old})}/2.
\end{aligned}
\tag{C3}
$$

The corresponding equations for the upper boundary are

$$
\begin{aligned}
w_x^{(\mathrm{new})} &= w_x^{(\mathrm{old})},\\
w_z^{(\mathrm{new})} &= -d_3^{(\mathrm{old})}/(2I_{\mathrm{f}}),\\
-p_1^{(\mathrm{new})} &= d_3^{(\mathrm{old})}/2.
\end{aligned}
\tag{C4}
$$

As the non-reflecting boundaries act solely on the wavefield components normal to the boundaries, steeply incident propagation directions are not sufficiently attenuated and we therefore use additional diffusive boundaries for better performance.